Air-bridged photonic crystal slabs at visible and near-infrared wavelengths

K. B. Crozier,[1] Virginie Lousse,[2,3] Onur Kilic,[3] Sora Kim,[3] Shanhui Fan,[3] and Olav Solgaard[3]
[1]*Division of Engineering and Applied Sciences, Harvard University, Cambridge, Massachusetts 02138, USA*
[2]*Laboratoire de Physique du Solide, Facultes Universitaires Notre-Dame de la Paix, 61 rue de Bruxelles, B-5000 Namur, Belgium*
[3]*E. L. Ginzton Laboratory, Stanford University, Stanford, California 94305, USA*
(Received 23 July 2005; revised manuscript received 15 February 2006; published 30 March 2006)

Air-bridged photonic crystal slabs are demonstrated at visible and near-infrared wavelengths. We present experimental and theoretical studies of the transmission spectra of air-bridged photonic crystal slabs with free space illumination using collimated and focused beams. We show that the resonances of an air-bridged photonic crystal slab exhibit considerable differences in their sensitivity to the angle of illumination. We show that the variation in the quality factor of a resonance with the incident angle of illumination is determined by the symmetry of its field distribution. Last, we present experimental and theoretical results on the transmission spectra of air-bridged photonic crystal slabs with focused illumination, important due to the finite angular spread of real optical beams.

DOI: 10.1103/PhysRevB.73.115126 PACS number(s): 42.70.Qs

I. INTRODUCTION

While most photonic crystal slab research has concentrated on compact devices suitable for planar chip-scale integration, air-bridged photonic crystal slabs illuminated with free-space beams present a number of advantages as filters, mirrors, and displacement sensors. As free-space optical filters, air-bridged photonic crystal slabs offer several improvements over conventional thin film dielectric filters. First, in a photonic crystal slab, a filtering function with an arbitrarily high quality factor can be in principle achieved with a single dielectric layer. By contrast, in traditional thin film filters, many dielectric layers are required to achieve high quality factor filter functions. For example, thin film filters used in wavelength division multiplexing (WDM) systems often have up to 100 dielectric layers with stringent tolerances on each layer.[1] The compactness of filters based on air-bridged photonic crystal slabs makes them easily incorporated into microelectromechanical systems (MEMS). Second, air-bridged photonic crystal slabs offer useful filtering functions, such as all-pass transmission and flattop reflection.[2] Third, the transmission and reflection spectra of a pair of closely spaced air-bridged photonic crystal slabs can be tuned by varying the spacing between the slabs,[3] for example, from all-pass transmission to flattop reflection.[4] It was recently theoretically shown that photon tunneling between coupled photonic crystal slabs enables high sensitivity displacement sensing.[5] Photonic crystal slabs also offer a means for realizing mirrors and for devices that provide significant group delay upon reflection and transmission (useful for delay lines and dispersion compensation). In addition, the freestanding nature of air-bridged photonic crystal slabs opens new opportunities for visible-wavelength optical sensors. Photonic crystal slabs can act as high quality factor optical resonators, with intense optical fields in the holes.[6] This field concentration would enhance the sensitivity of optical spectroscopy of gases and liquids that could be passed through the holes from one side of the slab to the other.

This paper includes three main contributions to photonic crystal slabs. First, air-bridged photonic crystal slabs are demonstrated at visible wavelengths. This wavelength range includes the important applications of microscopy, spectroscopy, imaging and displays. Our previous work on air-bridged silicon photonic crystal slabs was carried out at infrared wavelengths ($\lambda \approx 1.05-1.60\ \mu$m).[7,8] Kanskar *et al.*[9] demonstrated air-bridged photonic crystal slabs at near-infrared wavelengths ($\lambda \approx 0.91-1.28\ \mu$m). Second, we present experimental measurements of the transmission spectra of air-bridged photonic crystal slabs with the angle of incidence varied. This is very important, since the variation in the transmission spectrum with angle determines the fabrication and alignment tolerances of practical devices. Previous experimental demonstrations of air-bridged photonic crystal slabs[7–9] were carried out with normal-incidence illumination. Third, we present experimental and theoretical studies of the transmission spectra of air-bridged photonic crystal slabs with focused illumination. This work is important because the transmission and reflection spectra of photonic crystal slabs are strongly modified by the finite angular spreads of focused illuminating beams. Previous theoretical studies,[2–5,7,10–13] of air-bridged photonic crystal slabs used plane wave illumination, and did not consider focused illumination. Previous experimental demonstrations of air-bridged photonic crystal slabs used well-collimated illumination,[7–9] or focused illumination without the angular distribution specified.[9]

Optical filters based on one- and two-dimensional grating structures, known as guided resonance filters, have been previously demonstrated.[14–16] However, these devices are layered structures on solid substrates, unlike the devices presented in this paper, which consist of a single air-bridged dielectric layer. A broadband polarization-selective mirror has been experimentally realized at infrared wavelengths, in a structure consisting of a one-dimensional grating, a lower-index layer and a substrate.[17] Photonic crystals have been previously demonstrated at visible wavelengths.[18,19] However, these were planar waveguide structures, in contrast to our devices, which are air bridged for free-space illumination. Resonant features in the reflectivity spectra of two-dimensional photonic crystals have been previously observed at infrared wavelengths by Kanskar *et al.*[9] and Astratov *et al.*[20]

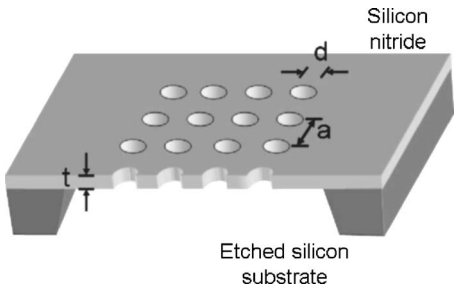

FIG. 1. Photonic crystal slab consisting of a square lattice of air holes etched into a freestanding dielectric thin film (silicon nitride). Slab parameters: thickness t, period a and hole diameter d.

The body of the paper begins with a discussion of the band structure and transmission spectrum of an air-bridged photonic crystal slab (Sec. II). The fabrication method for silicon nitride photonic crystal slabs is presented as Sec. III. In Sec. IV, experimental results and a theoretical method for the calculation of the transmission spectra of photonic crystal slabs with collimated and focused illumination are presented.

II. OPTICAL PROPERTIES OF AIR-BRIDGED PHOTONIC CRYSTAL SLABS

A. Organization of section

In this section, we consider the optical properties of air-bridged photonic crystal slabs at visible wavelengths. Band structures calculated by the finite difference time domain (FDTD) technique and the empty lattice approximation are shown in Sec. II B. In Sec. II C, we present calculations of the transmission spectra of photonic crystal slabs. The lower refractive indices of materials transparent at visible wavelengths lead to differences in the optical properties of photonic crystals fabricated from these materials, in comparison with previously reported, higher-index, infrared wavelength photonic crystal slabs.[2–5,7–13] These differences are discussed in Sec. II D.

B. Band structure of an air-bridged photonic crystal slab

An air-bridged photonic crystal slab consists of a two-dimensional periodic refractive index contrast introduced into a freestanding guiding layer. The device considered in this paper is illustrated as Fig. 1. A square lattice of circular holes is etched into a freestanding silicon nitride membrane on a silicon substrate.

To begin, we present the band structure of a photonic crystal slab with infinitesimally small holes as Fig. 2. This is useful to consider, as it can be calculated using an analytical technique known as the empty lattice approximation.[12] This method provides a solution against which numerical (FDTD) calculations can be checked, and is an intuitive physical model for the band structure. In Sec. II D, we use this model to predict the effects of lowering the slab refractive index. In the empty lattice approximation, photonic crystal band structures are interpreted as the modes of a uniform dielectric slab folded into the first Brillouin zone through Bragg scattering provided by the photonic crystal lattice. The dispersion curves of uniform dielectric slabs can be found from wave-

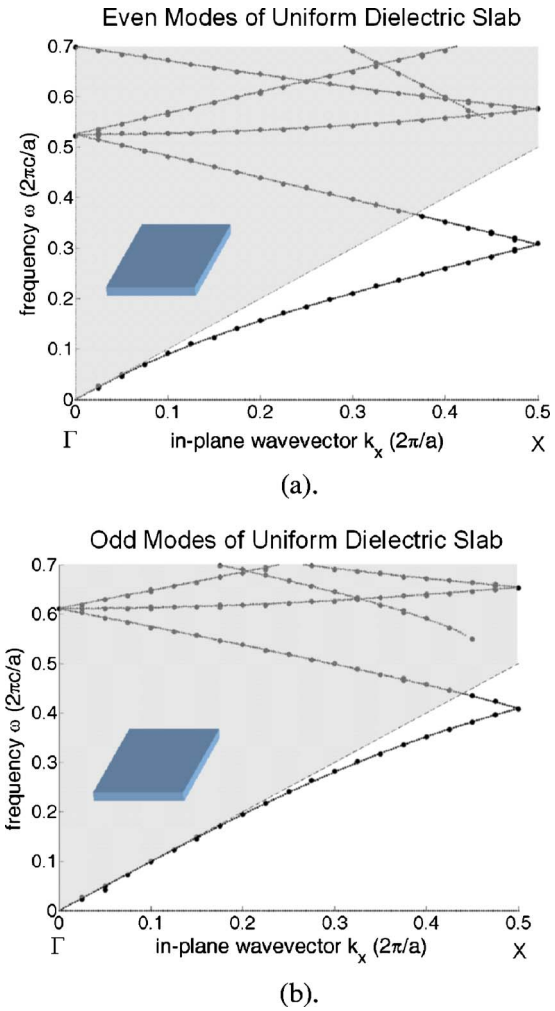

FIG. 2. (Color online) Band structure of photonic crystal slab with infinitesimally small holes (uniform dielectric slab). (a) Modes with field distributions that are even with respect to symmetry plane of slab. (b) Modes with field distributions that are odd with respect to symmetry plane of slab. Slab thickness $t=0.439a$, where a =period. Refractive index $n=2.282$. Solid lines: waveguide theory calculations. Solid dots: finite difference time domain (FDTD) calculations.

guide theory.[21,22] The dispersion curves are folded into the first Brillouin zone by adding reciprocal lattice vectors. In Fig. 2, the band structure found by the empty lattice approximation is shown using solid lines. The slab has a thickness of $0.439a$, period a, and a refractive index of 2.282. We plot the modes with electric field distributions whose in-plane components are even with respect to the mirror plane parallel to the slab as Fig. 2(a). The modes with odd symmetry are plotted as Fig. 2(b). In this figure, the in-plane wave vector is varied from the Γ point ($k_x=0$, $k_y=0$) to the X point ($k_x=\frac{\pi}{a}$, $k_y=0$).

For calculation of the band structures of air-bridged photonic crystal slabs with finite-sized holes, numerical methods such as FDTD are needed. In order to assess the accuracy of our FDTD implementation, we first compare it with the results of the analytical model. The modes of the slab found by FDTD are shown in Fig. 2 as solid dots. In the FDTD calculations, a dipole current source is placed in the slab to

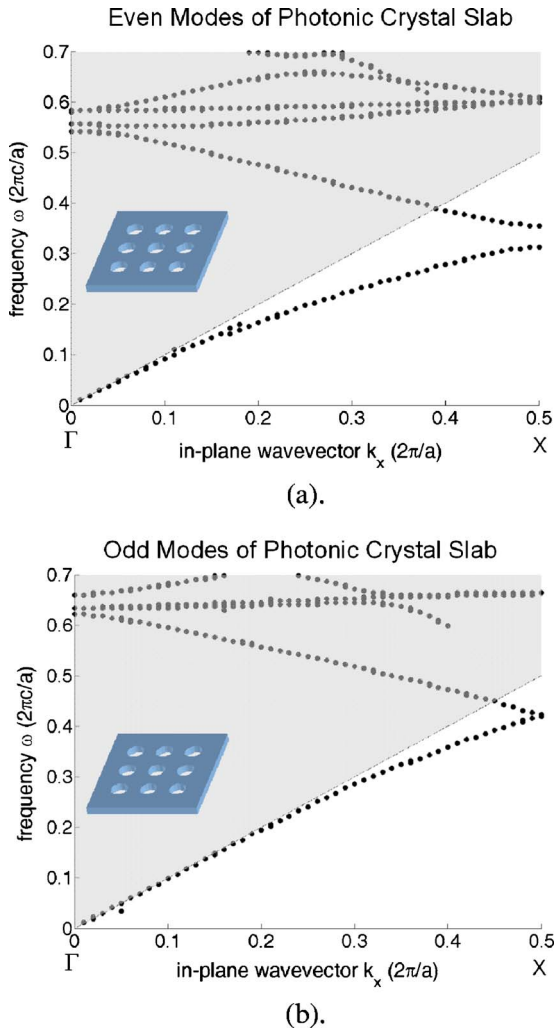

FIG. 3. (Color online) Band structure of photonic crystal slab. (a) Modes with field distributions that are even with respect to the symmetry plane of the slab. (b) Modes with field distributions that are odd with respect to the symmetry plane of the slab. Slab parameters: thickness $t=0.439a$, hole diameter $d=0.416a$, where a =period. Refractive index $n=2.282$.

excite its modes. The time evolution of the fields at randomly chosen points inside the slab is recorded and Fourier transformed to give the power spectra. The peaks in the power spectra give the frequencies of the modes of the slab. The in-plane wave vectors of these modes are set by the imposition of periodic boundary conditions in the x and y directions (i.e., in the plane of the slab). The computational regions above and below the slab are terminated in perfectly matched layers, thereby simulating a slab with free space above and below it. From Fig. 2, it can be seen that the FDTD method is in excellent agreement with the analytical method.

In Fig. 3, the band structure of an air-bridged photonic crystal slab with finite-sized holes is calculated by FDTD. The photonic crystal has periodicity a, thickness $0.439a$, hole diameter $0.416a$, and refractive index 2.282. These parameters are similar to the devices fabricated for this paper. For simplicity, these calculations do not include the effects of material loss or dispersion. Calculations including these effects are included later in this paper. From Fig. 3, it can be seen that the band structure of the photonic crystal slab with finite-sized holes is similar to the slab with infinitesimally small holes. However, the presence of the holes splits the fourfold degenerate state at the Γ point (for the slab with infinitesimally small holes) into a pair of doubly degenerate states and two singly degenerate states (for the slab with finite size holes). As discussed in Sec. IV, this has important consequences for the transmission and reflection spectra.

C. Normal-incidence transmission spectrum of an air-bridged photonic crystal slab

In this section, we calculate the normal-incidence transmission spectrum of an air-bridged photonic crystal slab. We discuss the relationship between the transmission spectrum and the band structure. We present calculations showing the effects of reducing the hole radius. We discuss applications of unique features of the spectral response of air-bridged photonic crystal slabs.

The transmission and reflection spectra of photonic crystal slabs with free-space illumination consist of sharp resonant features on a smooth Fabry-Pérot background. The physical origin of these resonant features can be understood by considering Fig. 2. The Bragg scattering provided by the photonic crystal lattice folds the modes of the dielectric slab into the first Brillouin zone. This brings modes above the light line, allowing them to be coupled to by free-space illumination. We refer to these modes as guided resonances.[10] The coupling of electromagnetic energy to guided resonances leads to sharp resonant features in the transmission and reflection spectra, as discussed below.

Electromagnetic energy incident upon the slab can couple to the guided resonances of the slab, or to the continuum of radiation modes, which are similar to the Fabry-Pérot oscillations of an unpatterned dielectric slab. Interference between these two pathways leads to transmission and reflection spectra with features known as Fano resonances.[23,35] In Fig. 4(a), the transmission spectrum is calculated for a photonic crystal slab with periodicity a, thickness $0.439a$, hole diameter $0.416a$, and refractive index 2.282 (the same parameters as that of Fig. 3). The calculations are performed using the transfer matrix method,[24] which is described in more detail in Sec. IV. The spectrum consists of sharp resonant features superimposed upon a smoothly varying background. In Fig. 4(b), the parameters are identical, except that the hole diameter is halved to $0.208a$. As discussed below, these spectra exhibit a number of interesting features, which make photonic crystal slabs useful as filters, mirrors and for generating group delay.

First, from Figs. 4(a) and 4(b), it can be seen that the quality factors of the resonances increase with decreasing hole size. This controllability of the linewidth is useful in filter applications by, for example, allowing the passband of a notch filter to be chosen. Second, in the vicinity of a resonance, the transmission varies between 0% and 100%. This is desirable in a number of applications. For example, a photonic crystal slab with a reflectance of 100% may be used as a mirror. By comparison, an unpatterned dielectric slab has a maximum normal-incidence power reflectance of $(n_2^2$

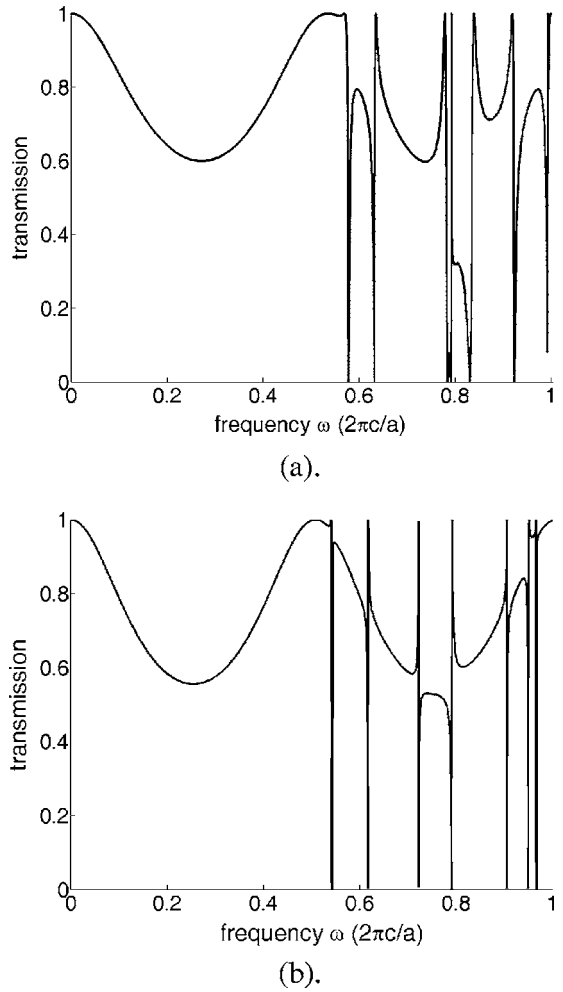

FIG. 4. (a) Calculated power transmission vs frequency of photonic crystal slab. Slab parameters: thickness $t=0.439a$, hole diameter $d=0.416a$, and refractive index $n=2.282$. (b) Same as (a), except that the hole diameter is $d=0.208$.

$-n_1^2)^2/(n_2^2+n_1^2)^2$, where n_2 and n_1 are the refractive indices of the slab and surrounding medium, respectively. For silicon nitride, for example, with a refractive index of 2.282, the maximum power reflectance is ~46%. Third, guided resonances generate significant optical delay. For a single resonance, there is a strong variation in the transmitted intensity as a function of wavelength. Recently, however, it was shown that, by careful design, unity transmission and a strong resonant delay can be achieved by a photonic crystal slab with two resonant modes with opposite symmetries and the same center frequencies and linewidths.[2] Devices with these characteristics are known as all-pass filters (APFs) and are useful as optical delay lines and for dispersion compensation.[25].

D. Effect of lowering the refractive index of the photonic crystal slab

Using the empty lattice approximation, we can show that lowering the slab refractive index reduces the number of modes of the photonic crystal slab. To do this, it is helpful to interpret a mode of the dielectric slab as a TE or TM wave

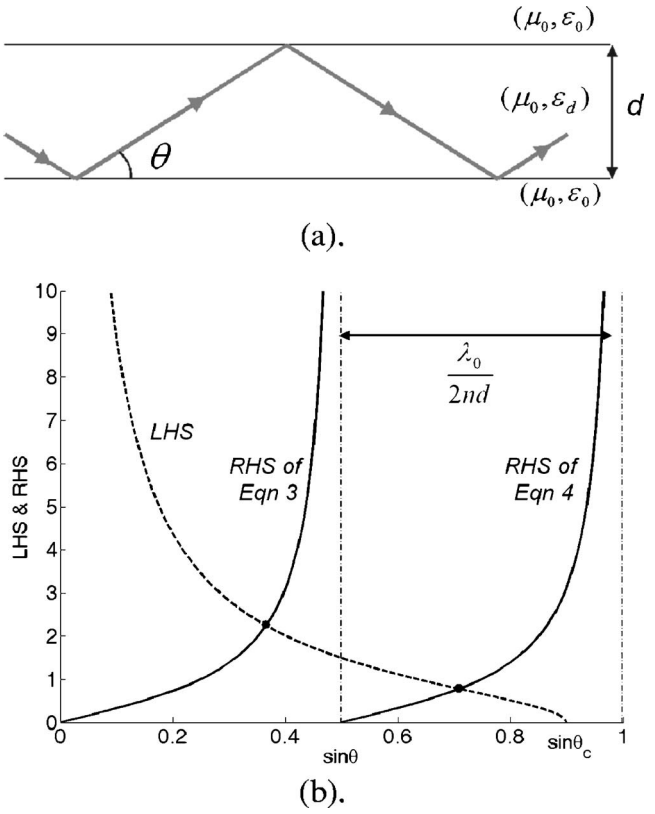

FIG. 5. (a) Mode of uniform dielectric slab interpreted as a plane wave bouncing at an angle θ. Slab permeability and permittivity are (μ_0,ε_d). Slab has free space (μ_0,ε_0) above and below it. Slab thickness is d. (b) Graphical solution for TE modes of uniform dielectric slab with $\varepsilon_d=5.21\varepsilon_0$ and $d=0.439a$. Left-hand sides (LHS) and right-hand sides (RHS) of Eqs. (3) and (4) are plotted as a function of sin θ. Solutions are shown as solid dots. Branches of tan( ) and −cot( ) are separated by $\lambda_0/(2nd)$.

bouncing between the slab surfaces at an angle θ.[26] For total internal reflection, θ must be smaller than the critical angle θ_c, as illustrated in Fig. 5(a). For a slab with refractive index n, θ_c is given by

$$\sin\theta_c = \sqrt{1-\frac{1}{n^2}}. \tag{1}$$

The bounce angle θ is given by

$$\sin\theta = \sqrt{1-\frac{\beta^2}{\omega^2\mu_0\varepsilon_d}}, \tag{2}$$

where β is the propagation constant, ε_d is the slab permittivity, and μ_0 is the permeability of free space.

The odd and even TE modes of the slab are found by solving[26]

$$\left(\frac{\sin^2\theta_c}{\sin^2\theta}-1\right)^{1/2} = \tan\left(\pi\frac{nd}{\lambda_0}\sin\theta\right) \tag{3}$$

and

$$\left(\frac{\sin^2\theta_c}{\sin^2\theta}-1\right)^{1/2}=-\cot\left(\pi\frac{nd}{\lambda_0}\sin\theta\right). \quad (4)$$

The left- and right-hand sides of Eqs. (3) and (4) are plotted in Fig. 5, with the solutions given by the intersection points, shown as solid dots. The slab refractive index n is 2.282, the thickness d is $0.439a$, and the frequency ω is $2\pi c/a$, corresponding to a normalized frequency ω' of 1. It can be seen that, at this frequency, the slab supports two TE modes at bounce angles given by $\sin\theta\approx 0.366$ and 0.709.

From inspection of Fig. 5, the effect of lowering the slab refractive index upon the number of modes of the uniform slab can be understood. The branches of *tan* and $-cot$ [right-hand side of Eqs. (3) and (4)] are spaced by $\lambda_0/(2nd)$, as shown in Fig. 5(b). Therefore, lowering n reduces the number of solutions within the range $0<\sin\theta<\sin\theta_c$. It should be noted that lowering n also reduces the value of $\sin\theta_c$, further reducing the number of modes of the uniform slab at a given frequency.

We can now use this model to predict the effect of lowering the refractive index upon the number of modes of the photonic crystal slab using the empty lattice approximation. We consider normal incidence (Γ point) for the frequency range $0<\omega'<1$. At the Γ point, the modes of the photonic crystal band structure are the modes of the uniform slab with propagation constants given by

$$\beta=\frac{2\pi}{a}\sqrt{p^2+q^2}, \quad (5)$$

where p and q are integers.

In order for the mode of the uniform slab to be propagating, the propagation constant β must be less than the maximum wave number in the dielectric, $(\omega/c)n$, which is equal to $(2\pi/a)\omega' n$. For a slab with a refractive index n of 2.282 and a normalized frequency ω' of 1, the propagation constant β can therefore take values of $\{\frac{2\pi}{a},\frac{2\pi}{a}\sqrt{2},\frac{2\pi}{a}\sqrt{4},\frac{2\pi}{a}\sqrt{5}\}$. To find the number of modes of the photonic crystal, we consider each value of the propagation constant in turn, and determine the range of $\sin\theta$ corresponding to the frequency range $0<\omega'<1$. We then determine the number of solutions with this range, for example, using the graphical solution of Fig. 5. For the photonic crystal with $n=2.282$ and $d=0.439a$, this results in 5 TE modes at the Γ point within the range $0<\omega'<1$.

For a photonic crystal slab with refractive index n of 3.46, the propagation constant β can take values of $\{\frac{2\pi}{a},\frac{2\pi}{a}\sqrt{2},\frac{2\pi}{a}\sqrt{4},\frac{2\pi}{a}\sqrt{5},\frac{2\pi}{a}\sqrt{8},\frac{2\pi}{a}\sqrt{9},\frac{2\pi}{a}\sqrt{10}\}$. For a slab thickness d of $0.439a$, this results in 15 TE modes, a significant increase over the number of modes of the slab with index $n=2.282$.

We therefore conclude that the lower refractive index of photonic crystal slabs at visible wavelengths leads to fewer modes. If needed, this can be compensated for by increasing the slab thickness since, as shown in Fig. 5, this increases the number of modes.

III. SILICON NITRIDE PHOTONIC CRYSTAL SLABS

The low loss and high index of silicon nitride at visible and near-infrared wavelengths make it suitable for photonic crystal slab devices in these spectral ranges. In addition, it has excellent mechanical properties. Silicon nitride can be deposited in smooth, uniform films by chemical vapor deposition or plasma-enhanced chemical vapor deposition. Silicon nitride films are generally pinhole free, making them commonly used as passivation layers in integrated circuits.

Scanning electron micrographs (SEMs) of the silicon nitride (Si_3N_4) photonic crystal slabs are shown as Figs. 6(a) and 6(b). The crystal occupies a square region of 100 μm $\times$ 100 μm, and is defined in a freestanding silicon nitride film. The starting substrate in the fabrication process is a double-side polished silicon wafer. Silicon nitride is deposited by low pressure chemical vapor deposition (LPCVD). Electron-beam lithography is used to define the photonic crystal patterns, which are plasma etched into the underlying silicon nitride film. Optical lithography is used to pattern the backside of the wafer, allowing square openings to be etched into the silicon nitride on the backside. The wafer is then etched in potassium hydroxide solution, resulting in freestanding silicon nitride square membranes.

IV. ANGULAR BEHAVIOR OF AIR-BRIDGED PHOTONIC CRYSTAL SLABS

A. Motivation and approach

The behavior of the transmission spectra of air-bridged photonic crystal slabs as a function of the incident angle is very important, since it determines the angular tolerances permitted in free-space device applications. In addition, as further discussed in Sec. V, it determines the behavior under focused illumination. In order to understand the angular behavior of photonic crystals, transmission measurements are made with the angle of incidence varied from 0 to 10°. We discuss a technique for calculating the transmission spectra of air-bridged photonic crystal slabs at arbitrary angles of incidence. Excellent agreement between theory and experiment is obtained.

B. Experimental results

The experimental setup used for transmission measurements at varying incident angles is shown as Fig. 7. Light from a xenon lamp is collimated (by lens L1) and focused (by lens L2) into a multi-mode optical fiber (O.F. 1). An order-sorting filter (FL) is placed between the collimation and focusing lenses. The light from the optical fiber is collected by a microscope objective lens (M.O. 1), passes through a polarizer (PL) and illuminates the photonic crystal (Ph.C.), which is mounted on a rotation stage (R.S.). The light transmitted through the crystal is collected by a second microscope objective (M.O. 2) and coupled to a second optical fiber (O.F. 2), which is multi-mode in the wavelength range used. The output of this optical fiber is input to an optical spectrum analyzer (O.S.A.). The transmission measurements presented in this paper are calculated by normalizing the spectra measured through the photonic crystal by the spectra measured with no sample in place. The spectra are measured over the wavelength range $\lambda=452-900$ nm.

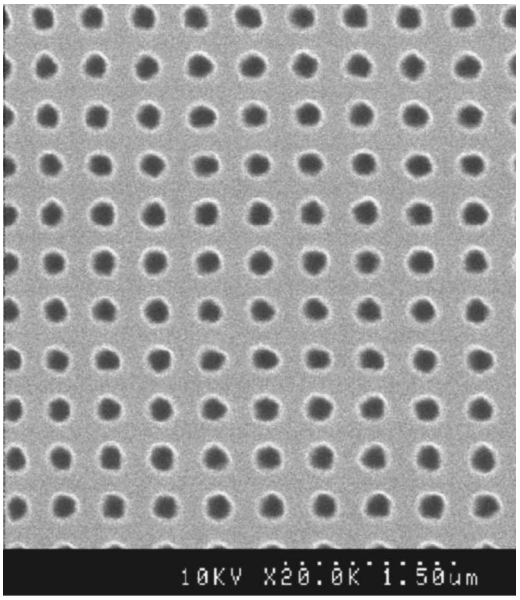

(a).

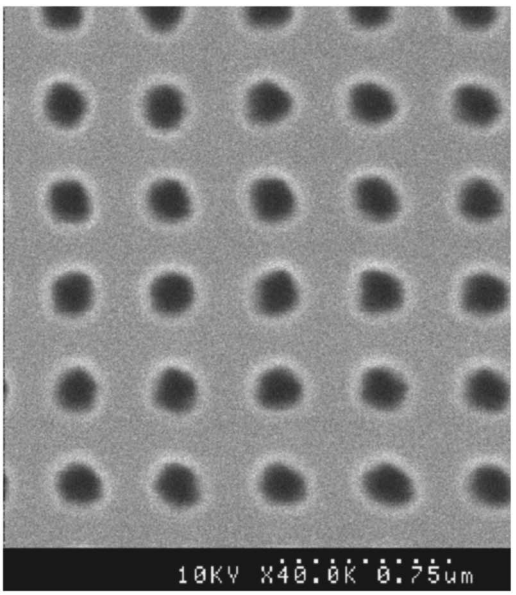

(b).

FIG. 6. (a) and (b) Scanning electron micrographs of silicon nitride photonic crystal slab. Slab parameters: thickness $t=196$ nm, period $a=452$ nm, hole diameter $d=190$ nm.

Experimental transmission spectra made at different angles of incidence with the electric field polarized in the plane of incidence are shown as Fig. 8. In Fig. 8(a), transmission spectra are presented for different angles of incidence, with the wavelength as the vertical scale, and the horizontal scale as the incident angle. The transmission is represented by a color scale, with dark blue corresponding to zero transmission (0%) and dark red corresponding to unity transmission (100%). These spectra are also presented in Fig. 8(b). In this plot, 11 spectra made at angles of incidence between 0 and 10° are shown. Figure 8(c) illustrates the orientation of electric (E), magnetic (H) and propagation (k) vectors of the incident plane wave with respect to the photonic crystal.

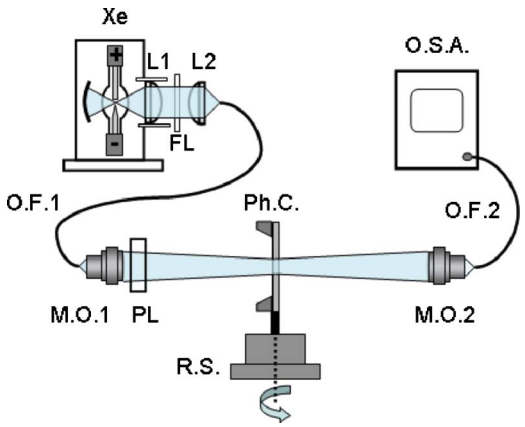

FIG. 7. (Color online) Experimental setup for transmission measurements of photonic crystal slab with adjustable angle of incidence of illumination. Xe—xenon lamp, L1—lamp collimation lens, FL—filter, L2—fiber coupling lens, O.F. 1 and 2—optical fibers, M.O. 1–2—microscope objectives, Ph.C.—photonic crystal, O.S.A—optical spectrum analyzer, P.L.—polarizer, R.S.—rotation stage.

Experimental results for the photonic crystal transmission as a function of incident angle with the electric field vector perpendicular to the plane of incidence are shown as Fig. 9. Figure 9(c) illustrates the orientation of the electric (E), magnetic (H) and propagation (k) vectors of the incident plane wave with respect to the photonic crystal. Due to the different polarization of the illumination beam, different resonances are coupled to, compared to the results of Fig. 8.

C. Discussion

The transmission spectra of Figs. 8(a), 8(b), 9(a), and 9(b) exhibit a number of important features. First, some resonances [e.g., resonance near $\lambda=760$ nm in Fig. 8(a)] display little variation in width and position (wavelength) as the incident angle is varied from 0 to 10°. On the other hand, some resonances increase in wavelength [e.g., resonance near $\lambda=700$ nm in Fig. 8(a)] whereas others decrease in wavelength [e.g., resonance near $\lambda=670$ nm in Fig. 8(a)] as the incident angle is increased. This behavior is explained in this section through consideration of the band structure. Second, the depths of some of the resonances vary appreciably with incident angle [e.g., resonance near $\lambda=670$ nm in Fig. 8(a)], while for other resonances [e.g., resonance near $\lambda=760$ nm in Fig. 8(a)], there is little variation with incident angle. This behavior is explained in section IV E.

The variation in the wavelength of a resonance with incident angle can be understood by considering the photonic crystal band structure. As shown in Figs. 2 and 3, in a band structure diagram, the frequencies of the modes are plotted as a function of the in-plane wave vector. With free-space illumination, modes above the light line in the band structure can be coupled to, and appear in the transmission spectrum as Fano line shapes on a Fabry-Pérot background. As dis-

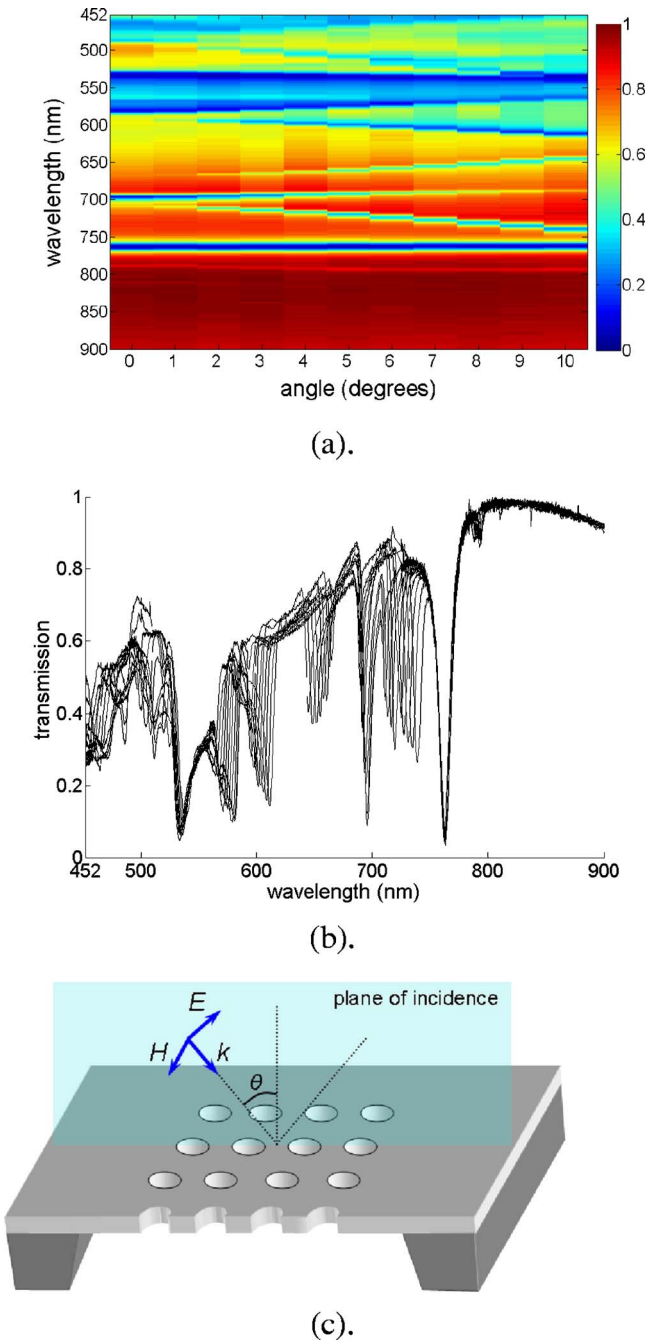

FIG. 8. (Color online) Measured transmission vs angle of incidence (θ) for polarization in the plane of incidence: (a) color plot, (b) spectra, (c) schematic of photonic crystal showing definition of θ. E, H and k: electric field vector, magnetic field vector, and propagation vector of illumination, respectively.

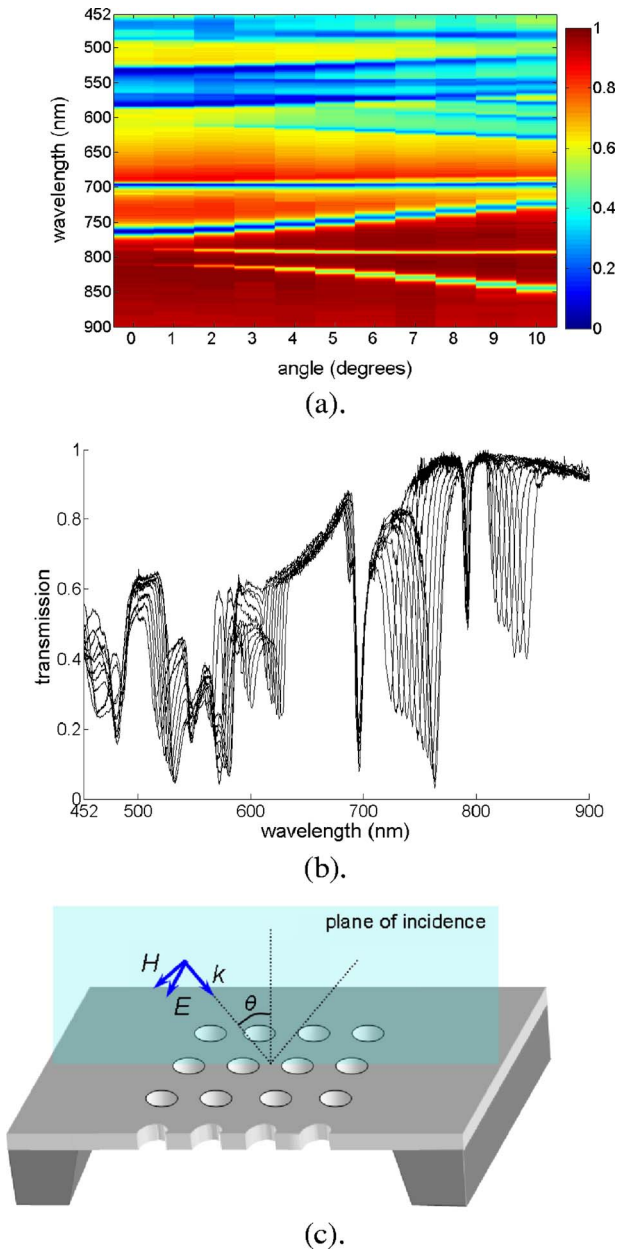

FIG. 9. (Color online) Measured transmission vs angle of incidence (θ) for polarization perpendicular to plane of incidence: (a) color plot, (b) spectra, (c) schematic of photonic crystal showing definition of θ. E, H and k: electric field vector, magnetic field vector, and propagation vector of illumination, respectively.

cussed further in Sec. IV E., however, in order for a mode to be coupled to, the symmetry of its field distribution must match that of the illumination. Therefore, not all modes of the band structure appear in the transmission spectrum. A mode that is coupled to at an incident angle θ and wavelength λ appears in the band structure at an in-plane wave vector of

$$k_x = \frac{2\pi}{\lambda} \sin \theta \tag{6}$$

and a normalized frequency ω' of

$$\omega' = \frac{a}{\lambda}. \tag{7}$$

As discussed, some resonances increase in wavelength with incident angle, while others decrease in wavelength. This can be understood from the empty lattice approximation. In Fig. 10, we consider the bands resulting from the translation of the mode of a uniform slab (curve I) by one

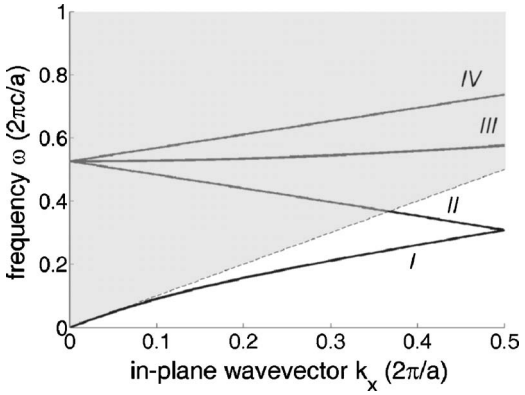

FIG. 10. Band structure of photonic crystal slab with infinitesimally small holes (uniform dielectric slab), with four bands plotted. Curve I is the lowest-order TE mode of slab. Curves II–IV result from the translation of Curve I by up to one reciprocal lattice vector in the x and y directions. Slab thickness $t=0.439a$, where a is period. Slab refractive index is 2.282.

reciprocal lattice vector $(2\pi/a)$ in x and y directions. Let us denote the dispersion relation of the uniform slab mode by $\omega_U(\beta)$, where β is the propagation constant. The photonic crystal band structure is then given by

$$\omega_{\mathrm{PhC}}(k_x,k_y) = \sum_{p=-\infty}^{\infty}\sum_{q=-\infty}^{\infty} \omega_U \times\left(\beta = \sqrt{\left(k_x + p\frac{2\pi}{a}\right)^2 + \left(k_y + q\frac{2\pi}{a}\right)^2}\right). \tag{8}$$

In Fig. 10, k_x varies from 0 to π/a and $k_y=0$. Curve I corresponds to the lowest-order TE mode of a uniform slab prior to translation, so that $p=0$ and $q=0$. Curves II-IV result from translation of curve I by $-2\pi/a$ in the x direction ($p=-1$, $q=0$, curve II), $\pm 2\pi/a$ in the y direction ($p=0$, $q=\pm 1$, curve III) and $2\pi/a$ in the x direction ($p=1$, $q=0$, curve IV). The lowest-order TE mode (curve I) increases monotonically in frequency with in-plane wave vector. Therefore, curves III and IV increase in frequency with in-plane wave-vector k_x because their propagation constants β [see Eq. (8)] also increase with wave-vector k_x. On the other hand, curve II decreases in frequency with k_x because β decreases with k_x. It can also be noted that the increase in ω of curve III over the range $k_x=0$ to π/a is less than that of curve IV because the increase of β over that range is lower for curve III than IV. Therefore, it can be concluded that the observation that the resonances increase, decrease or remain fairly flat in wavelength with incident angle can be understood through the empty lattice approximation.

D. Numerical modeling

The goal of this section is to present a method for the calculation of the transmission and reflection spectra of air-bridged photonic crystal slabs for polarized illumination at arbitrary angles of incidence. As discussed, the variation of the transmission and reflection spectra with incident angle is important, as it determines the angular alignment tolerances and the behavior under focused illumination. We have previously demonstrated a method for finding the transmission spectra of air-bridged photonic crystal slabs at arbitrary angles of incidence,[7] but did not compare the numerical predictions with experimental results. Fan and Joannopoulos[10] calculated the transmission spectra of photonic crystal slabs using FDTD for the case of a fixed in-plane wave-vector k_x. In such calculations, the incidence angle changes with frequency ω according to Eq. (12). By comparison with FDTD, the technique presented here allows the transmission spectrum to be computed for a fixed incident angle. We compare the numerical calculations with experimental results.

The simulations have been performed with a momentum-space version of the transfer-matrix method. The method has been well documented in the literature[27,28] and widely used.[29–32] Here we briefly summarize the main idea. In this approach, the fields are represented by a linear combination of plane waves with wave vector parallel to the film surfaces. Due to the periodic nature of the system, the wave vectors of these plane waves are restricted to a discrete set as specified by the Bloch conditions. By further choosing only those plane wave components with a small Bloch wave number, the representation becomes finite. In the calculations, convergence is reached by including a sufficient number of plane wave components. The amplitude for each plane wave component varies with the coordinate z which represents the depth in the structure, normal to the film surfaces. For each plane wave component, we distinguish between the incoming and outgoing wave amplitudes. The scattering matrix (S matrix) of the entire system relates the outgoing wave amplitude to the incoming wave amplitude on either side of the film. In order to calculate the S matrix of the film, we divide the film into N segments perpendicular to the film. The S matrix for each segment is determined by solving Maxwell's equations directly inside the segment. Within each segment, the solution of the S matrix becomes relatively simple when the size of the segment is sufficiently small. The total S matrix is then constructed by cascading the S matrix from each segment, using the multiple scattering formula familiar in the theory of low-energy electron diffraction.[33] As emphasized in Ref. 28, doing so avoids the numerical instability related to the presence of evanescent waves in this class of method. The knowledge of the total S matrix solves the scattering problem and gives the transmission and reflection coefficients.

Using this approach, calculations of the photonic crystal slab transmission are made at incident angles from 0 to 10° for light polarized in the plane of incidence (Fig. 11) and normal to the plane of incidence (Fig. 12). In the calculations, the photonic crystal period a is 452 nm, the hole diameter 190 nm, and the slab thickness 196 nm. These parameters are chosen to match those of the fabricated device. The hole diameter is determined by scanning electron microscopy, and has a standard deviation of 13 nm. The slab thickness is determined by ellipsometry, and has a standard deviation of 1 nm. The photonic crystal period is the design value used in the electron beam lithography step. The standard deviation of the photonic crystal period has not been measured directly, but is estimated to be 6 nm. This estimate

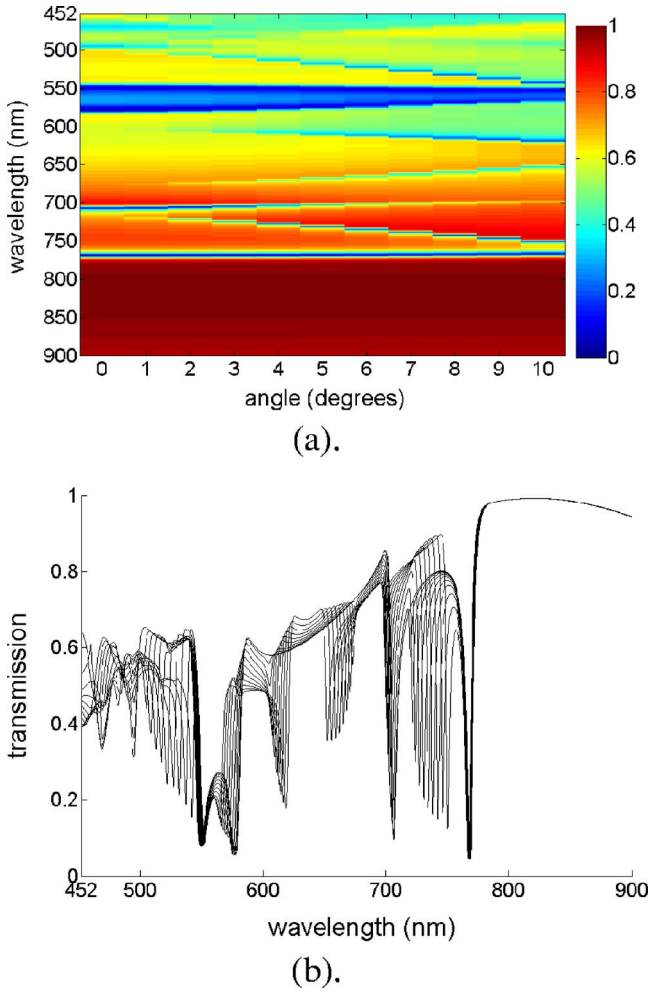

FIG. 11. (Color online) Theoretical transmission vs angle of incidence (θ) for polarization in the plane of incidence: (a) color plot, (b) spectra.

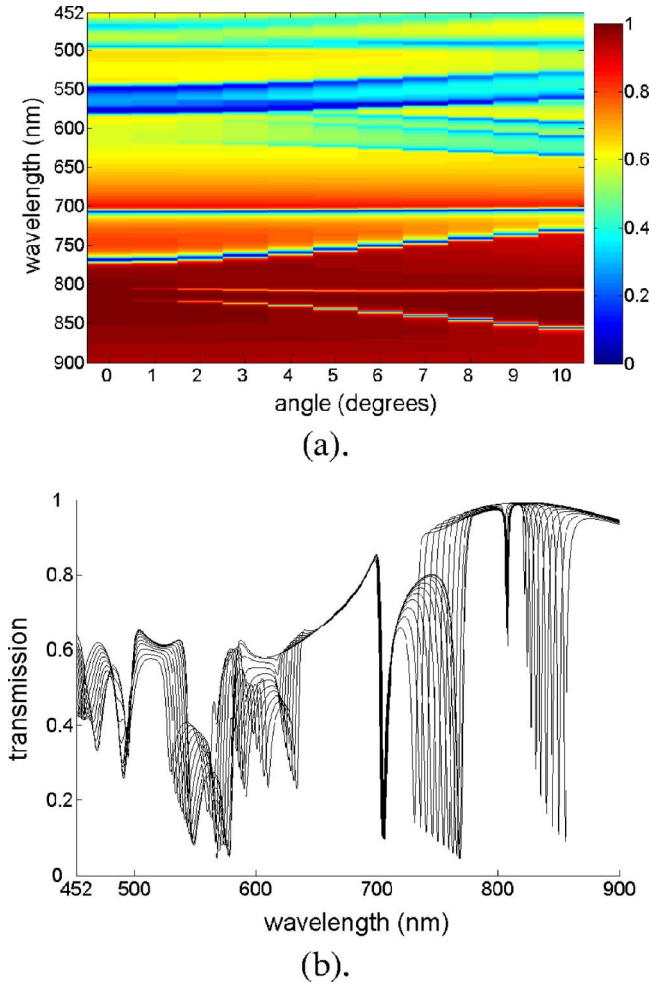

FIG. 12. (Color online) Theoretical transmission vs angle of incidence (θ) for polarization perpendicular to plane of incidence: (a) color plot, (b) spectra.

is made by assuming that the standard deviation in the hole period is 1.4% of the hole period, based on our previous study,[8] in which we found standard deviations of 1.1%–1.4% of the hole period for silicon photonic crystal slabs fabricated using the same electron beam lithography machine. The real (n) and imaginary (k) parts of the silicon nitride refractive index are found from transmission measurements made on unpatterned membranes. It should be noted that the absorption loss of silicon nitride could be further reduced by increasing its nitrogen content.[34]

By comparing the theoretical spectra of Figs. 11 and 12 with the experimental results shown as Figs. 8 and 9, it can be seen that our numerical method is in very good agreement with experimental results for both polarizations of the illumination. It can be seen that the positions, widths and depths of the resonances calculated by the transfer matrix method match the experimental data very well. The results demonstrate the ability of the transfer matrix method to model accurately the transmission spectra of air-bridged photonic crystal slabs.

The numerical calculations assume identical and circular holes. From Fig. 6, however, it is apparent that, in fabricated devices, the holes are not perfectly circular and vary in diameter. This nonuniformity might be expected to add a mechanism for scattering loss, which would lower the quality factors of the resonances and decrease their depth. However, this is not seen to be the case, with the experimental measurements (Figs. 8 and 9) being in very good agreement with calculations made for photonic crystals with perfectly circular and identical holes (Figs. 11 and 12). Therefore, it can be concluded that scattering loss from imperfections does not affect the transmission spectra greatly, or that the effect is small compared with absorption loss.

E. Resonance symmetry and coupling: Discussion

The purpose of this section is to explain an observation made on the experimental data, namely that there are two distinct patterns of behavior in the strength of coupling to a resonance as the illumination angle is varied. For some resonances, the coupling to the resonance is very strong at normal incidence, as evidenced by a strong dip in transmission. For other resonances, the coupling is very weak at normal incidence, as evidenced by a small dip is transmission. We show that this behavior is determined by the symmetry of the

resonance. This phenomenon has been previously predicted theoretically.[10,11,12] It has been observed experimentally for two-dimensional AlGaAs photonic crystals[35] although, unlike our devices, these photonic crystals were not air bridged, but fabricated on substrates. We previously identified[8] features in the normal incidence transmission spectrum of an air-bridged silicon photonic crystal slab as singly degenerate modes, but in that investigation we did not vary the incident angle. Here, we experimentally observe the variation in the coupling to different resonances as a function of incident angle.

Both the experimental data and numerical simulations exhibit two distinct patterns of behavior as the incident angle is varied, as discussed above. For some resonances (e.g., resonance of Fig. 9 with $\lambda=763$ nm at normal incidence), the dip in transmission becomes large as the angle of incidence approaches zero. On the other hand, for some resonances (e.g., resonance of Fig. 9 approaching $\lambda=789$ nm at normal incidence), the dip in transmission becomes very small as the angle of incidence approaches zero. In other words, some resonances (e.g., $\lambda=763$ nm resonance) are strongly coupled to at normal incidence (resulting in a large dip in transmission), whereas other resonances (e.g., $\lambda=789$ nm resonance) are very weakly coupled to at normal incidence.

These two distinct patterns of behavior can be understood by considering the symmetries in the field patterns of these resonances. In Fig. 13, the electric field distributions in the mirror plane parallel to the slab are plotted for several modes. The plots are of the instantaneous values of the in-plane electric fields, with the field amplitude denoted by a color scale, and the direction of the field given by the arrow direction. The field distributions are found using the plane-wave expansion method.[36] This method assumes periodicity in all three dimensions. The photonic crystal slabs in this paper, however, are periodic in two dimensions only, with free space above and below the slab. Nevertheless, the fields in the slab may be accurately computed using this method provided that the slab separation (given by the periodicity in the direction normal to the plane of the slab) is sufficiently large. When this is the case, the field distribution in the slab is largely unaffected by the presence of slabs above and below it, as the slabs are in the far field of each other.

In Figs. 13(a) and 13(b), the electric field distributions of the degenerate modes with frequency 0.5835 ($2\pi c/a$) are plotted. In Fig. 13(c), the field distributions of the singly degenerate mode with frequency 0.5572 ($2\pi c/a$) is plotted. In these calculations, the slab parameters are: thickness $0.434a$, period a, and hole diameter $0.420a$. The slab refractive index is 2.282. The slab parameters are almost identical to the slab of Fig. 3. The modes of Fig. 13 therefore appear in the band structure of Fig. 3, and are even modes.

The degenerate modes of Figs. 13(a) and 13(b) appear in the experimental data as pronounced dips in transmission at $\lambda\sim763$ nm. The singly degenerate mode of Fig. 13(c) appears in the experimental data as the mode at $\lambda\sim789$ nm that is very weakly coupled to, as evidenced by the weak dip in transmission. Examination of the symmetries of the distributions of Fig. 13 explains the observed behavior. Because the photonic crystal structure is symmetric for reflection about the x, y, and z axes, the field components must have

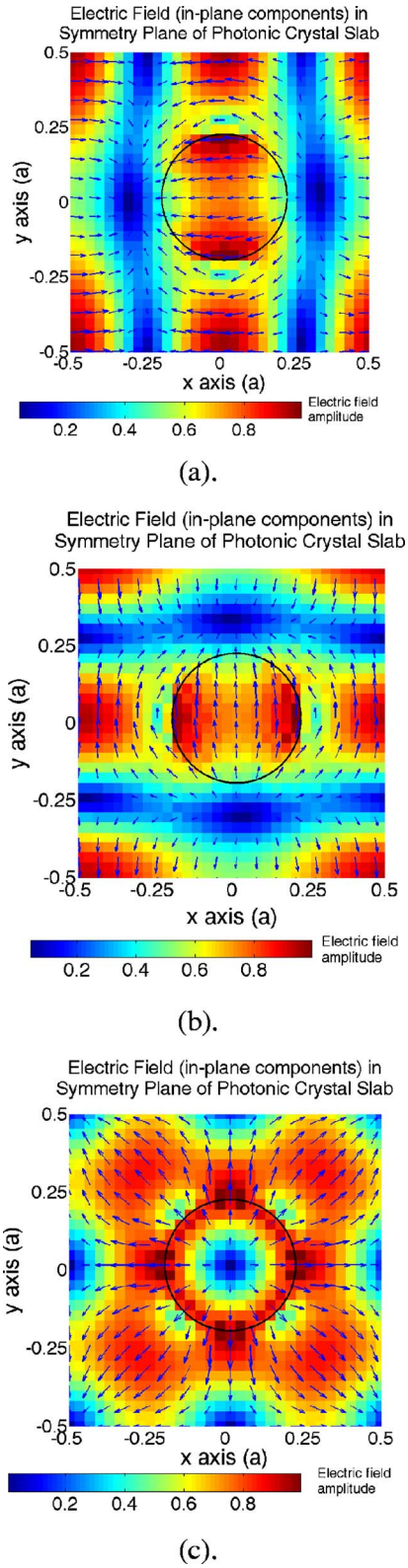

FIG. 13. (Color online) Electric field distributions (in-plane components) in the symmetry plane of a photonic crystal slab. Slab parameters: thickness$=0.434a$, diameter$=0.420a$, where a is period. Slab refractive index is 2.282. (a) and (b) Degenerate modes with frequency 0.5835, (c) singly degenerate mode with frequency 0.5572. Circumference of hole is shown as a solid line.

odd or even symmetries for reflections about these planes. For example, the mode shown as Fig. 13(a) possesses even parity for reflections about the x axis, and odd parity for reflection about the y axis. This mode is therefore able to couple to a plane wave propagating normal to the slab that has its electric fields polarized in the x direction, as such a plane wave has the same parity as the mode. Similarly, the mode shown as Fig. 13(b) possesses even parity for reflections about the y axis and odd parity about the x axis. It is therefore able to couple to a plane wave propagating normal to the slab that has its electric field polarized in the y direction, as such a plane wave has the same parity as the mode. On the other hand, the singly degenerate mode shown as Fig. 13(c) has even parity about both x and y axes. It is therefore unable to couple to plane waves propagating normal to the slab. It is therefore expected that there be zero coupling to this mode, and that it should not appear in the normal-incidence transmission spectrum. In the experimental data, this mode is very weakly coupled to, as evidenced by the small dip in the transmission spectrum at $\lambda \sim 789$ nm. This nonzero coupling is likely to be due to the finite angular spread of the illuminating beam, which leads to illumination of the photonic crystal slab at nonnormal incidence. The singly degenerate modes can be excited by free-space radiation when the illumination is not at normal incidence. In this case, the in-plane wave vector of the mode is finite, and there is no longer a symmetry mismatch between it and a plane wave. Imperfections of the crystal may also contribute to the finite coupling that we observe. Nevertheless, it is clear that the coupling to this mode is very weak, especially by comparison to the modes at $\lambda \sim 763$ nm, and that the coupling becomes progressively weaker as the angle of incidence approaches zero. It can be therefore concluded that the two distinct patterns of coupling behavior result from the differences between modes in their field symmetries.

V. TRANSMISSION SPECTRA OF AIR-BRIDGED PHOTONIC CRYSTAL SLABS WITH FOCUSED ILLUMINATION

A. Organization of section

In this section, we present experimental results and a theoretical method for calculating the transmission spectra of air-bridged photonic crystal slabs that are illuminated with focused beams. To the best of our knowledge, this has not been previously reported for air-bridged photonic crystal slabs. Theoretical studies have been carried out on the performance of guided-mode filters as a function of beam width and device size.[37,38] These devices consist of one-dimensional gratings. As discussed in Sec. I, a number of filter and displacement sensor devices have been proposed that employ air-bridged photonic crystal slabs, but these designs have assumed plane-wave illumination. As illustrated in Fig. 14, a focused beam has a finite angular spread, and therefore illuminates the photonic crystal with a distribution of plane waves of different angles of incidence and polarization states. It is therefore important to determine the influence of this finite angular spread upon the performance of the photonic crystal. In Sec. V B, we present experimental results on the transmission spectra of air-bridged photonic crystal slabs with focused illumination. In Sec. V C, we present a method for calculating the photonic crystal slab transmission with focused beam illumination. The experimental results and theoretical predictions are found to be in good agreement.

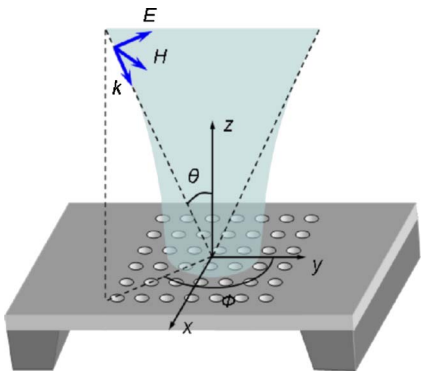

FIG. 14. (Color online) Illustration of converging-beam illumination of photonic crystal. E, H, k—electric field, magnetic field, and propagation vectors of a ray incident on the photonic crystal at (θ, Φ).

B. Transmission spectrum with focused illumination: Experimental results

The experimental setup used is shown as Fig. 15. It is similar to that of Fig. 7, but with an additional pair of lenses and an adjustable iris that allow the photonic crystal to be illuminated by a beam with an adjustable convergence angle. Light from a xenon lamp is collimated (L1), filtered (FL) and focused (L2) into an optical fiber (O.F.1). The light from the optical fiber is then collected by a microscope objective (M.O.1) and then forms a waist at the tube length. The beam expanding away from the tube length is then passed through an adjustable iris (A.I.) and through a second microscope objective (M.O. 2), which focuses it onto the photonic crystal (Ph.C.). The light transmitted through the photonic crystal is then collected by a third microscope objective (M.O.3) and then focused by a fourth objective (M.O.4) into an optical

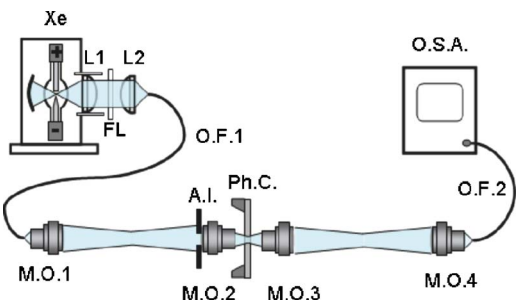

FIG. 15. (Color online) Experimental setup for transmission measurements of photonic crystal slab where convergence angle of focused illumination beam on the photonic crystal can be adjusted. Xe—xenon lamp, L1—lamp collimation lens, FL—filter, L2—fiber coupling lens, O.F. 1 and 2—optical fibers, M.O. 1–4—microscope objectives, A.I.—adjustable iris aperture, Ph.C.—photonic crystal, O.S.A—optical spectrum analyzer.

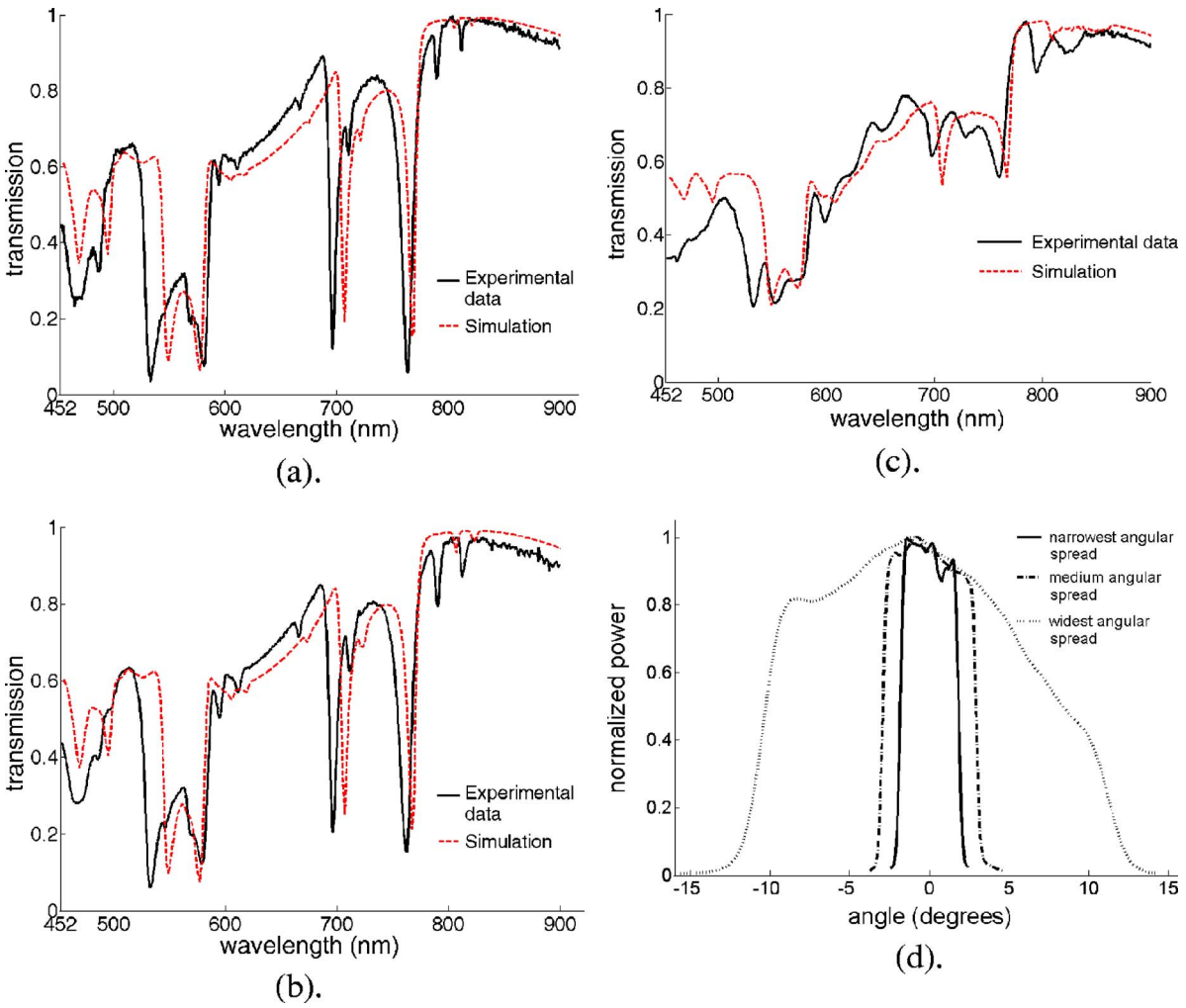

FIG. 16. (Color online) Transmission spectra under converging-beam illumination of a photonic crystal slab. Black solid line—measured transmission spectra. Red dashed line—calculated transmission spectra. Transmission spectra with (a) narrowest convergence angle, (b) medium convergence angle, (c) widest convergence angle. (d) Normalized power vs angle for the three different beams used in measurements of parts (a)–(c).

fiber (O.F.2). The output of the optical fiber is input to an optical spectrum analyzer (O.S.A). The adjustable iris allows control of the convergence angle of the beam illuminating the photonic crystal.

Transmission spectra are shown as Fig. 16. Experimental spectra are plotted as solid black lines, and calculated spectra are shown as dashed red lines. The experimental transmission spectrum of Fig. 16(a) is obtained for a beam with a convergence angle of approximately 2°. Compared to the results shown previously, it can be seen that the depths of the resonances are slightly shallower, due to the increased angular spread of the illumination. In Fig. 16(b), the convergence angle of the illumination is increased to approximately 3°. From the experimental data, it can be seen that the depths of the resonances are markedly reduced. In Fig. 16(c), the convergence angle is increased to approximately 11°. The experimental transmission spectrum is significantly altered due to this increased angular spread, with the depths of the resonances being much less than before. In Fig. 16(d), the measured angular distributions of the power in the illuminating beams used in parts (a)–(c) are shown. These are obtained by measuring the power transmitted by a pinhole scanned in a direction transverse to the beam propagation direction, in the far field of the beam (away from the beam focus). This allows the normalized power as a function of angle to be found.

C. Transmission spectrum with focused illumination: Theoretical model

As discussed, it is expected that increasing the convergence angle of the beam decreases the depth of the resonances and broadens them, as it is equivalent to illuminating the photonic crystal with plane waves at a number of different incident angles and polarization states and averaging the response. The resonance wavelength will be in general different for each of these angles, so we expect that the summation of the waves at these angles will decrease the depth of the resonance. In order to study this, numerical calculations are made of the transmission spectra for beams with convergence angles approximating those used in the experiments. As discussed, the results are shown as dashed red

curves in Figs. 16(a)–16(c). As shown in Fig. 16(d), the angular distributions of the beams used in the experiments are not symmetric or smooth. For the calculations of Fig. 16, the angular distributions are approximated as top-hat functions, with unity normalized power for $0<\phi<360°$ and $\theta<\theta_{\max}$. The maximum illumination angle $\theta_{\max}$ is taken as 2°, 3° and 11° for the calculations of Figs. 16(a)–16(c), respectively. The transmission spectra are found by calculating the power transmission of plane waves at a number of angles over the range $0<\phi<360°$ ($\phi=0°,10°,20°,\ldots,80°$) and $\theta<\theta_{\max}$ ($\theta=0°,1°,\ldots,\theta_{\max}$), and then averaging these spectra.

The theoretical calculations of Figs. 16(a)–16(c) are in good agreement with the experimental data. As before, the depths of the resonances decrease as the convergence angle of the beam is increased. The calculated and measured spectra of Figs. 16(a) and 16(b) are in good agreement. The widest convergence angle illumination of Fig. 16(c) exhibits the expected reduction in the resonance depth, though the match with the experimental data is not as good as for the two cases with the beams with smaller convergence angle. This may be due to the simplified angular distribution taken for the calculations. The real beam for this case was clearly nonuniform and not symmetric, as shown in Fig. 16(d). The good agreement between theory and experiment confirms that the transfer matrix method may be used to predict the photonic crystal slab response under converging-beam illumination.

The theory and experiments with converging-beam illumination allow us to estimate the minimum size required of the photonic crystal. If the illumination is a Gaussian beam, then the angular divergence of the beam is given by[26]

$$\theta_0 = \frac{2}{\pi}\frac{\lambda}{2W_0}, \tag{9}$$

where λ is the wavelength and $2W_0$ is the waist diameter, also called the spot size. Taking a wavelength of 633 nm and a divergence angle of 1° gives a spot size of ~23 μm. Therefore, the photonic crystal needs to be only approximately this size to achieve a filtering function at least as good as the results of Fig. 16(a) (which were measured for illumination with a convergence angle of 2°). This confirms that photonic crystal slab devices can be very compact and still achieve useful functionality as free-space optical components.

VI. CONCLUSIONS

This work provides the experimental demonstration of Fano resonances in air-bridged photonic crystal slabs at visible wavelengths. Being able to operate in this spectral range is of critical importance to applications in spectroscopy, microscopy, imaging and displays. We provide the experimental measurements of the transmission spectra of air-bridged photonic crystal slabs with the incident illumination angle varied. The results clearly demonstrate that the transfer matrix method can be used to determine the transmission of the photonic crystal slab under varying angle of illumination and polarization state. Last, we provide the experimental and theoretical studies of the optical properties of air-bridged photonic crystal slabs with focused illumination. The results show that air-bridged photonic crystal slab devices can be very compact, making them useful as free-space filters, mirrors, and sensors.

ACKNOWLEDGMENTS

V.L. was supported as a postdoctoral researcher by the Belgian National Fund for Scientific Research (FNRS). Fabrication work was carried out in the Stanford Nanofabrication Facility, which is partially funded by the National Science Foundation.

[1] H. A. Macleod, Proc. SPIE **4094**, 46 (2000).
[2] W. Suh and S. Fan, Appl. Phys. Lett. **84**, 4905 (2004).
[3] W. Suh, M. F. Yanik, O. Solgaard, and S. Fan, Appl. Phys. Lett. **82**, 1999 (2003).
[4] W. Suh and S. Fan, Opt. Lett. **28**, 1763 (2003).
[5] W. Suh, O. Solgaard, and S. Fan, J. Appl. Phys. **98**, 033102 (2005).
[6] J. M. Pottage, E. Silvestre, and P. St. J. Russell, J. Opt. Soc. Am. A **18**, 442 (2000).
[7] V. Lousse, W. Suh, O. Kilic, S. Kim, O. Solgaard, and S. Fan, Opt. Express **12**, 1575 (2004).
[8] O. Kilic, S. Kim, W. Suh, Y. A. Peter, A. S. Sudbo, M. F. Yanik, S. Fan, and O. Solgaard, Opt. Lett. **29**, 2782 (2004).
[9] M. Kanskar, P. Paddon, V. Pacradouni, R. Morin, A. Busch, J. F. Young, S. R. Johnson, J. MacKenzie, and T. Tiedje, Appl. Phys. Lett. **70**, 1438 (1997).
[10] S. Fan and J. D. Joannopoulos, Phys. Rev. B **65**, 235112 (2002).
[11] P. Paddon and J. F. Young, Phys. Rev. B **61**, 2090 (2000).
[12] T. Ochiai and K. Sakoda, Phys. Rev. B **63**, 125107(R) (2001).
[13] T. Ochiai and K. Sakoda, Phys. Rev. B **64**, 045108 (2001).
[14] R. Magnusson and S. S. Wang, Appl. Phys. Lett. **61**, 1022 (1992).
[15] S. Tibuleac and R. Magnusson, J. Opt. Soc. Am. A **14**, 1617 (1997).
[16] S. Peng and G. Michael Morris, Opt. Lett. **21**, 549 (1996).
[17] C. F. R. Mateus, M. C. Y. Huang, L. Chen, C. J. Chang-Hasnain, and Y. Suzuki, IEEE Photonics Technol. Lett. **16**, 1676 (2004).
[18] M. C. Netti, M. D. B. Charlton, G. J. Parker, and J. J. Baumberg,

Appl. Phys. Lett. **76**, 991 (2000).
[19] J. J. Baumberg, N. M. B. Perney, M. C. Netti, M. D. C. Charlton, M. Zoorob, and G. J. Parker, Appl. Phys. Lett. **85**, 354 (2004).
[20] V. N. Astratov, I. S. Culshaw, R. M. Stevenson, D. M. Whittaker, M. S. Skolnick, T. F. Krauss, and R. De La Rue, J. Lightwave Technol. **17**, 2050 (1999).
[21] D. K. Cheng, *Field and Wave Electromagnetics* (Addison–Wesley, Reading, MA, 1990).
[22] H. A. Haus, *Waves and Fields in Optoelectronics* (Prentice–Hall, Englewood Cliffs, NJ, 1984).
[23] S. Fan, W. Suh, and J. D. Joannopoulos, J. Opt. Soc. Am. A **20**, 569 (2003).
[24] J. B. Pendry and A. MacKinnon, Phys. Rev. Lett. **69**, 2772 (1992).
[25] G. Lenz and C. K. Madsen, J. Lightwave Technol. **17**, 1248 (1999).
[26] B. E. A. Saleh and M. C. Teich, *Fundamentals of Photonics* (Wiley, New York, 1991).
[27] J. B. Pendry and A. MacKinnon, Phys. Rev. Lett. **69**, 2772 (1992).
[28] J. B. Pendry, J. Mod. Opt. **41**, 209 (1994).
[29] M. Sigalas, C. M. Soukoulis, E. N. Economou, C. T. Chan, and K. M. Ho, Phys. Rev. B **48**, 14121 (1993).
[30] E. Özbay, G. Tuttle, M. Sigalas, C. M. Soukoulis, and K. M. Ho, Phys. Rev. B **51**, 13961 (1995).
[31] J. S. McCalmont, M. M. Sigalas, G. Tuttle, K. M. Ho, and C. M. Soukoulis, Appl. Phys. Lett. **68**, 2759 (1996).
[32] M. M. Sigalas, K. M. Ho, R. Biswas, and C. M. Soukoulis, Phys. Rev. B **57**, 3815 (1998).
[33] J. B. Pendry, *Low Energy Electron Diffraction* (Academic, London, 1974).
[34] A. Kiermasz and K. Beekman, Semicond. Int. **13**, 108 (1990).
[35] V. Pacradouni, W. J. Mandeville, A. R. Cowan, P. Paddon, J. F. Young, and S. R. Johnson, Phys. Rev. B **62**, 4204 (2000).
[36] S. G. Johnson and J. D. Joannopoulos, Opt. Express **8**, 173 (2001).
[37] J. M. Bendickson, E. N. Glytsis, T. K. Gaylord, and D. L. Brundrett, J. Opt. Soc. Am. A **18**, 1912 (2001).
[38] E. Bonnet, X. Letartre, A. Cachard, A. V. Tishchenko, and O. Parriaux, Opt. Quantum Electron. **35**, 1025 (2003).